Simulation and optimization of a new focusing polarizing bender for the diffuse neutrons scattering spectrometer DNS at MLZ

K Nemkovski[1], A Ioffe[1], Y Su[1], E Babcock[1], W Schweika[2] and Th Brückel[2]

[1]Jülich Centre for Neutron Science (JCNS) at Heinz Maier-Leibnitz-Zentrum (MLZ), Forschungszentrum Jülich GmbH, Lichtenbergstr. 1, 85748 Garching

[2]Jülich Centre for Neutron Science (JCNS) und Peter Grünberg Institut (PGI), JARA-FIT, Forschungszentrum Jülich GmbH, Lichtenbergstr. 1, 524258 Jülich, Germany

k.nemkovskiy@fz-juelich.de

Abstract. We present the concept and the results of the simulations of a new polarizer for the diffuse neutron scattering spectrometer DNS at MLZ. The concept of the polarizer is based on the idea of a bender made from the stack of the silicon wafers with a double-side supermirror polarizing coating and absorbing spacers in between. Owing to its compact design, such a system provides more free space for the arrangement of other instrument components. To reduce activation of the polarizer in the high intensity neutron beam of the DNS spectrometer we plan to use the Fe/Si supermirrors instead of currently used FeCoV/Ti:N ones. Using the VITESS simulation package we have performed simulations for horizontally focusing polarizing benders with different geometries in the combination with the double-focusing crystal monochromator of DNS. Neutron transmission and polarization efficiency as well as the effects of the focusing for convergent conventional C-benders and S-benders have been analyzed both for wedge-like and plane-parallel convergent geometries of the channels. The results of these simulations and the advantages/disadvantages of the various configurations are discussed.

1. Introduction

DNS is a versatile diffuse neutron scattering instrument with polarization analysis operated by JCNS at the research reactor FRM II (Heinz Maier-Leibnitz Zentrum) [1, 2]. It is used for studies of highly frustrated spin systems, strongly correlated electrons, emergent functional materials and soft condensed matter.

The general layout of the DNS is shown in figure 1. During the last years the instrument has been considerably upgraded. In particular, supermirror coating of the neutron guide (1) has been changed from m=1.2 to m=2. Respectively, the flux for the short-wavelength range has been considerably enhanced. The available short wavelength range has been extended from 2.4 Å to 1.5 Å. In order to deal with increased neutron flux, the monochromator (2) shielding has been replaced and improved. In addition, a neutron velocity selector (3) has been installed and successfully commissioned. The velocity selector allows suppressing the high-order contamination of the monochromatized beam

coming from double-focusing PG monochromator (2). Alternatively, the selector can be used for selecting a shorter wavelength by the PG004 reflection with better resolution and without moving the secondary spectrometer. For the purpose of inelastic scattering experiments recently we have successfully installed a new high-frequency disc chopper (5) enabling the time-of-flight operation mode (in commissioning).

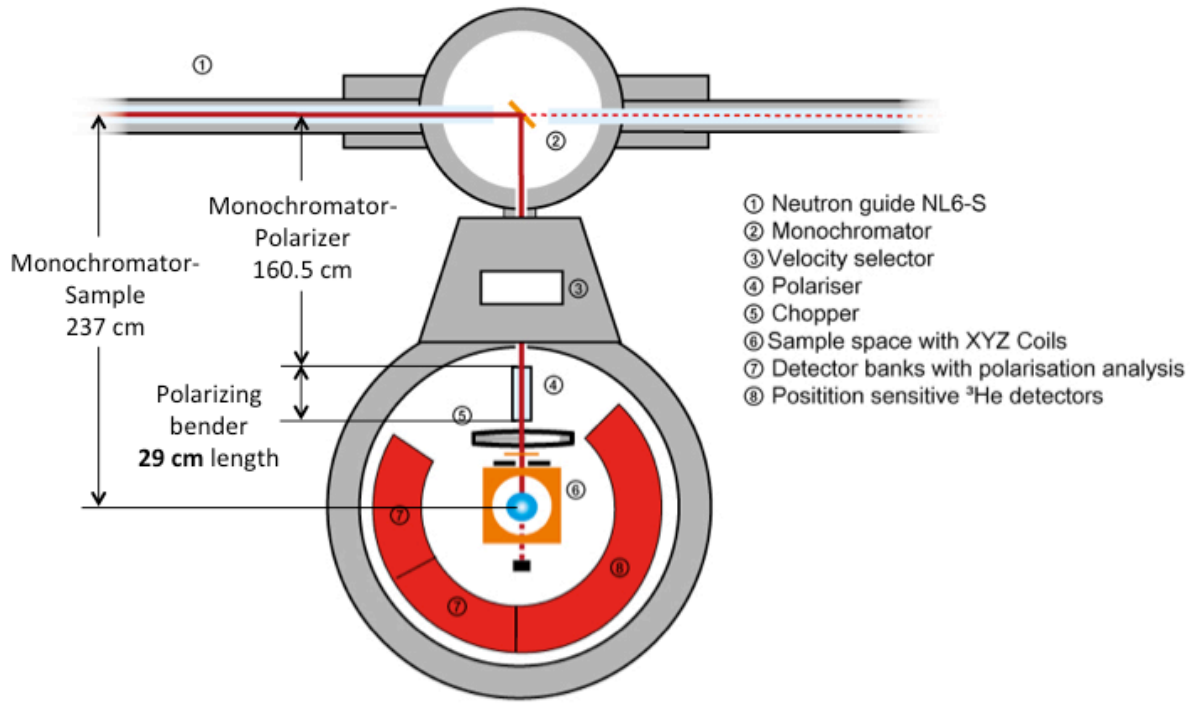

Figure 1. General layout of the diffuse neutron scattering spectrometer DNS at MLZ.

The polarization analysis at DNS is realized by a polarizer (4), XYZ-coils (6) with a Mezei-flipper and a polarization analyzer installed in the front of the detector bank (7). The currently used polarizer is a focusing Schärpf-type bender [3,4] of 29 cm length. It is composed of a stack of boron-containing glass sheets separated by wedge-type Al spacers. The spacers are essentially hollow sheets for optimal transmission, with only 6 mm Al material in trajectory of the neutrons. The glass sheets are coated on both sides by polarizing FeCoV/Ti:N supermirrors with a Gd:Ti anti-reflection layer underneath [5, 6]. To match the extended wavelength range, in the next step of the instrument upgrade we plan to change the existing polarizer.

The concept of the new polarizer is based on the idea of a solid-state bender composed of a number of silicon wafers with a double-side supermirror polarizing coating separated by absorbing spacers [7]. With this approach one can design very compact devices [7-10], which allows us to free space necessary for other instrument elements in the sample area. Additionally, to reduce the activation of the polarizer we plan to use the Fe/Si supermirrors [11] instead of currently used FeCoV/Ti:N ones. The optimization of the parameters of such a polarizing bender is the subject of this paper.

2. Analytical relations between bender parameters

Different geometries of benders impose certain constraints and relations between bender parameters, which can be easily obtained analytically and are presented below:

2.1. C-bender

In the case of a simple C-bender with plane-parallel channels (see figure 2a), the minimum length allowing avoiding the direct sight of view is given by

$$L_1^C = \sqrt{8Rd} \quad (1),$$

where R is the radius of curvature and d is the thickness of the channel ($R \gg d$) [12]. If the bender length L exceeds L_1^C, each neutron is reflected inside the channel at least once.

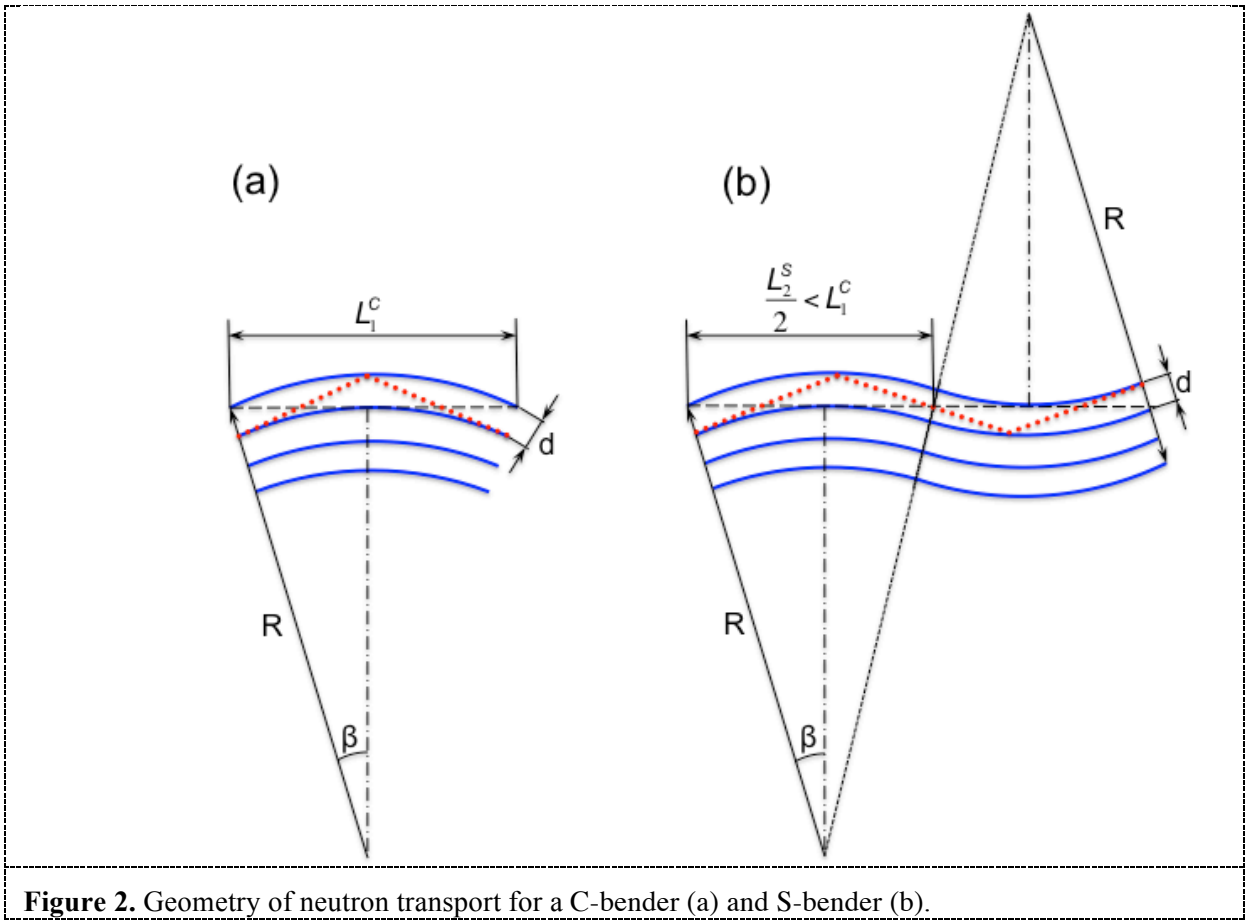

Figure 2. Geometry of neutron transport for a C-bender (a) and S-bender (b).

Another important parameter is the characteristic angle:

$$\beta = \sqrt{\frac{2d}{R}} \quad (2).$$

The value of 2β is sometimes referred as the bending angle of C-bender. It is also closely related to the characteristic shortest wavelength transmitted by the bender:

$$\lambda^* = \frac{\beta}{\gamma_c m} = \frac{1}{\gamma_c m}\sqrt{\frac{2d}{R}} \quad (3),$$

where $\gamma_c = 0.0017$ rad/Å is the critical angle of Ni coating for λ=1 Å, m is the index of the supermirror coating. Here one has to note, that for the C-bender there is no real cut-off value. Neutrons with shorter wavelength $\lambda<\lambda^*$ still can be transmitted by the C-bender (the so-called garland reflections), though their amount diminishes fast.

The equations (1-3) can be generalized to the case of convergent or divergent C-bender:

$$L_1^C = \sqrt{2Rd_1} + \sqrt{2Rd_2} \quad (4),$$

$$\beta = \sqrt{\frac{d_1}{2R}} + \sqrt{\frac{d_2}{2R}} \quad (5),$$

where d_1 and d_2 is width of the channel at the entrance and the exit, respectively ($|d_1 - d_2| \ll d$). By combining equations (3) and (5) one can see that for the convergent bender λ^* shifts towards a higher value, whereas for divergent bender it is just opposite.

2.2. S-bender

In the S-bender (see figure 2b) each neutron reflects inside the channel at least twice. The corresponding minimum length is given by:

$$L_2^S = 2\left(1+\sqrt{2}\right)\sqrt{Rd} \quad (6),$$

The characteristic angle β coincides with the one for the C-bender (see Eq. 2), however, here it is not anymore related to the deflection of the polarized beam with respect to the incoming beam: for an S-bender incoming and outgoing beams are parallel. However, β is still an important parameter that defines the transmitted wavelength range. Though in the case of an identical curvature and channel width the value of λ^* is the same both for C- and S-benders, the S-bender provides a sharp cut-off that strictly limits the minimum wavelength value:

$$\lambda_{cut-off} = \frac{2}{3}\lambda^* \quad (7).$$

The effect of the wavelength cut-off is illustrated in figure 3.

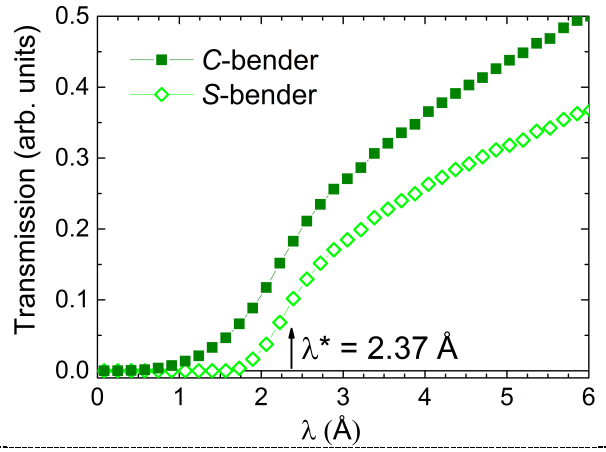

Figure 3. Transmission of the polarizing *not-convergent C-* and *S*-bender as a function of neutron wavelength as obtained from VITESS simulation. The parameters of both benders are based on the present-day geometry: d = 0.8 mm, R = 13500 mm. L = 300 and 510 mm for C- and S-bender, respectively. Transmission is normalized to the value for C-bender at λ = 6 Å.

The generalization for the case of convergent or divergent bender can be carried out in the same way as it is done in the section 2.1 (equations 4-5).

3. Monte-Carlo simulations

To optimize the parameters of the future polarizing bender for DNS, we have performed a series of Monte-Carlo simulations using the VITESS package [13]. Our model includes the cold source, the neutron guide, the double-focusing crystal monochromator (7x5 pieces of PG, 2.5 cm × 2.5 cm each, 0.55° mosaicity) and different kinds of polarizing benders. The main parameters for the options discussed in this paper are listed in Table 1.

The goal of simulations is to optimize the neutron beam parameters, flux and polarization, at the sample position. The neutron source has been simulated using the standard module "source_FRM2" from the VITESS library. In this module a simplified analytical description of the moderator characteristics is used, so that the resulted neutron spectrum slightly differs from the real one. Therefore, all intensity-related parameters are shown below in arbitrary units. In turn, the neutron wavelength dependences those are not normalized to the incoming flux, though being rather close to the expected in reality, are not completely accurate.

The reflectivity of the supermirror coating for the desired *m*-values is obtained by extrapolating the available data from Swiss Neutronics [14]. For solid state benders with Fe/Si coating, the position of the threshold at small Q in the spin-down reflectivity has been additionally corrected for the shift in the critical reflection angle caused by the difference in the refraction indices of the supermirror and the material of the bender channel (supermirror substrate), because the reflectivity curves in [14] have been obtained for neutrons incident from vacuum whereas in the case of the solid-state bender it is silicon). More details on the influence of the neutron-transmitting material on the reflectivity can be found in [11].

The neutron transmission of single-crystalline silicon has been taken into account according to data from [15]. The effect of the Laue extinction (the loss of the transmitted beam intensity by Bragg scattering in Si wafers) in the wavelength range of interest (i.e. 2-6 Å) is limited by the few narrow dips around 2.42, 2.79, and 5.06 Å, respectively [8]. During the measurements these particular wavelength values can be easily avoided. Therefore, for simplicity of the simulation we neglected the effect of Laue extinction.

Table 1. Main parameters of the simulated benders.

Style	Present-day air-gap C-bender	Solid-state C-bender, with wedge-type channels	Solid-state C-bender, with plane-parallel channels	Solid-state S-bender, with wedge-type channels	Solid-state C-bender, with plane-parallel channels
Length (mm)	290	55	55	95	95
Radius of curvature (mm)	13500	236	236	236	236
Channel width at the entrance (mm)	0.80	0.157	0.150	0.162	0.150
Channel width at the exit (mm)	0.57	0.150	0.150	0.150	0.150
Thickness of spacer between channels at the entrance (mm)	—	—	0.007	—	0.012
Thickness of absorbing layer (mm)	0.21	0.002	0.002	0.002	0.002
Supermirror coating	FeCoV/Ti:N m=2.7	Fe/Si m=3.5	Fe/Si m=3.5	Fe/Si m=3.5	Fe/Si m=3.5
Thickness of supermirror coating (mm)	0.003	0.003	0.003	0.003	0.003
Number of channels	44	271	271	265	265

Here we do not consider the air-gap C-bender with the Fe/Si coating instead of the FeCoV/Ti:N, because, first, it would not allow us to achieve a compact design – one of main objectives for a new polarizer and, second, having the same transmission for the desired spin state, it does not provide sufficiently high polarization for the whole required wavelength range.

The reason for the latter is the following. For a given wavelength, the maximal reflection angle for neutrons transmitted through the channel of bender is limited by the critical angle of the supermirror coating. The minimal angle is determined by the half of the bending angle β defined in equation 5 (some neutrons reflected by the angle smaller than $\beta/2$ still can pass through due to the garland reflections). On the other side, below critical reflection angle of Fe(↓)/Si the reflectivity for the Fe/Si coating is equal for both spin states that results in a low polarization at small incident angles (see figure 4). For neutrons incident to the supermirror from Si, the region of low polarization extends up to $\Theta \approx 0.8\gamma_C\lambda$. However, for neutrons incident from vacuum (or from air) it is increased to $\Theta \approx 0.8\gamma_C\lambda$. Obviously, the consequences of such shift are most severe for long wavelength neutrons. For instance, neutrons with $\Theta/(\gamma_C\lambda) = 0.5$ will be still well polarized (about 90%) when being incident from Si, and will not be polarized at all when being incident from vacuum. Indeed, in the latter case neutrons with wrong spin component will admix to the transmitted beam reducing its overall polarization. Simulations show that the beam polarization drops below 80% for $\lambda = 6$ Å - the upper limit of our wavelength range of interest.

To fix this problem one can decrease the radius of curvature by 2.5-3 times (to shift up the value of $\beta/2$, see equation 5) with the simultaneous increase of the critical angle of the supermirror coating to approximately 4.5 (to keep the value of λ^*, see equation 3). However, the length of such a bender will be about 170 mm, so that it will not be as compact as the solid state benders listed in table 1.

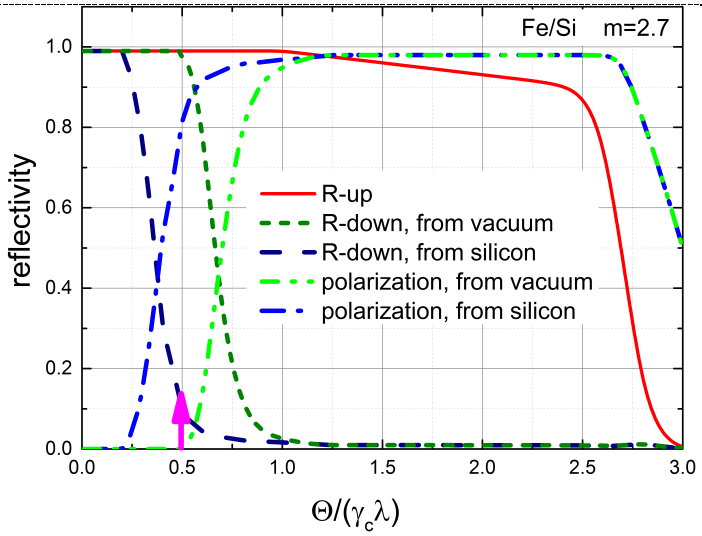

Figure 4. Model reflectivity for spin-up $|\uparrow\rangle$ and spin-down $|\downarrow\rangle$ states and polarization of m=2.7 Fe/Si supermirror vs. the normalized reflection angle. Reflectivity for the $|\downarrow\rangle$ component and polarization are shown for the neutron beam incidence from vacuum and silicon. The arrow indicates the position of the characteristic angle $\beta/2$ for $\lambda = 6$ Å.

3.1. Present-day configuration

As the first step we have simulated the present-day configuration of DNS, a combination of an Schärpf-type polarizer and the focusing monochromator. The distribution of the neutron beam intensity for the typical wavelength of 4.2 Å at different positions along the beam is shown in figure 5a-d. One can see that though the key element of the focusing system is the focusing monochromator, an essential role is also played by the bender. If we exclude the polarizing bender from our consideration, the beam width at the sample position (frame (d)) appears several times larger, because the bender does not accept the full horizontal divergence provided by the monochromator. Interestingly, at the same time the bender serves as the additional wavelength filter, because the most horizontally diverging neutrons also have the largest deviation in the wavelength. As a result (compare figures 5(e) and (f)), the bender reduces the wavelength spread and the beam divergence nearly by

factor of 2 (at $\lambda = 4.2$ Å). This effect is most pronounced for long wavelengths and less important for the short ones.

The important consequence of this analysis is that for the proper optimization of the polarizing bender it is crucial to consider it in the combination with the monochromator.

Further results for the present-day configuration (transmission, polarization and quality factor as a function of wavelength) are discussed in the next section in the comparison with other bender options.

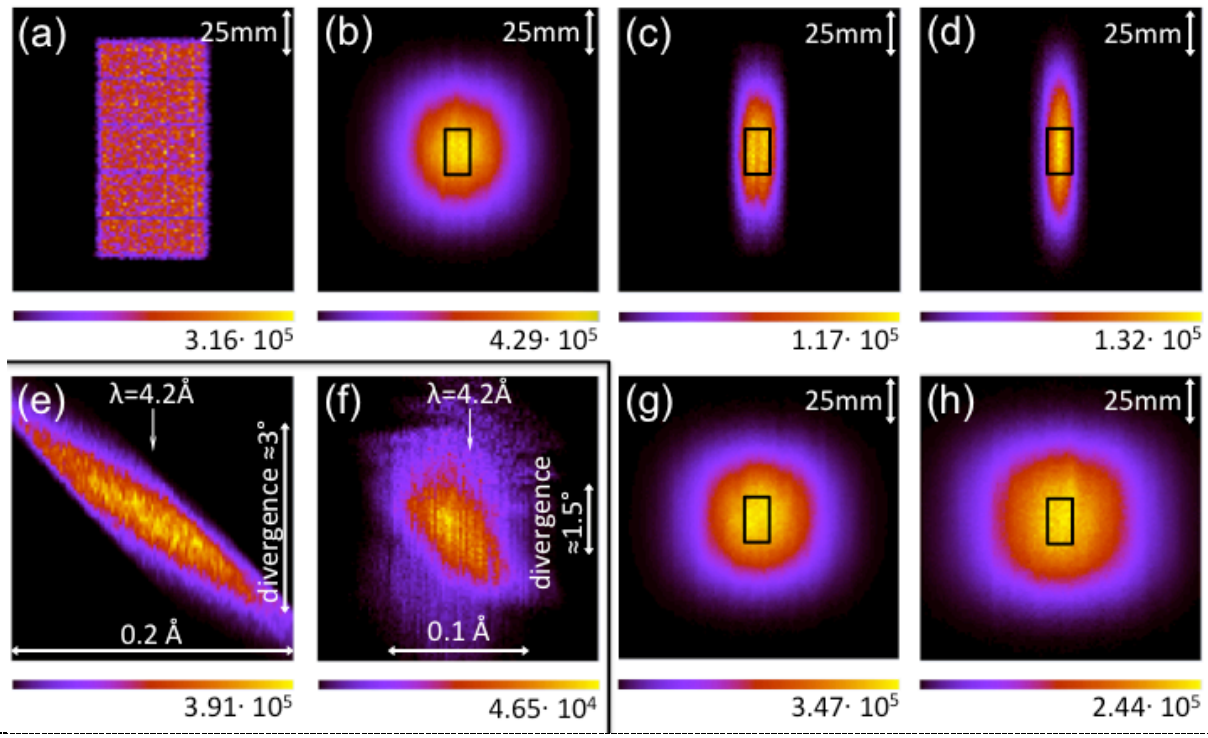

Figure 5. VITESS simulation of the present-day configuration of DNS (see text) at $\lambda = 4.2$ Å.
(a-d): Distributions of the neutron intensity across the beam at the (a) positions after monochromator, (b) entrance to the polarizing bender, (c) exit of the polarizing bender, (d) sample position.
(e,f): Neutron beam divergence vs. wavelength at the entrance (e) and the exit (f) of polarizing bender.
(g,h): Neutron intensity at the same positions as (c) and (d), respectively, but without bender.
The black rectangular in frames (a-d) and (g,h) corresponds to the image of one PG crystal of the monochromator.

3.2. Optimization of parameters of a new bender

To find the optimal supermirror coating index m for a new bender we have used the analytical relations (3) and (5). Using the parameters given in Table 1, one can obtain the characteristic wavelength for the present-day bender: $\lambda^* = 2.38$ Å. With a new polarizing bender we plan to expand the available wavelength range down to ~2 Å, which requires $m \geq 3.2$ for the same geometry. To be on the safe side, we have chosen slightly higher value of m=3.5.

The next important aspect is the arrangement of the bender channels. The current air-gap bender uses convergent wedge-type channels (see figure 6a). However, for the compact solid-state bender the production of silicon wedges of the necessary size is technologically very complicated. Therefore, as the main option we consider a bender with plane-parallel Si channels and spacers in between (figure 6b). Obviously, the part of the neutron beam entering the bender between Si wafers will be lost according to the ratio of the channel width to the spacer thickness. However, for a given inclination

angle between wafers the spacer thickness is in turn proportional to the bender length, so that in the case of the compact bender the losses should not be really significant.

For the purpose of quantitative comparison we have carried out the simulations for the currently installed air gap bender, and C- and S-benders of different geometries shown in figure 6: using wedge-type Si wafers (a), plane-parallel Si wafers separated by spacers at the entrance (b).

The distance from focusing monochromator to bender, as well as the total entrance width and the angle of total bender convergence are fixed according to the given DNS layout: 1605 mm, 45 mm and 2°, respectively. The width of the bender channel, i.e. the silicon wafers' thickness, is 150μm according to the present-day technological possibilities. The radius of curvature and the length of benders are scaled from the present-day geometry using equations (4, 5). Parameters used for simulations are listed in Table 1.

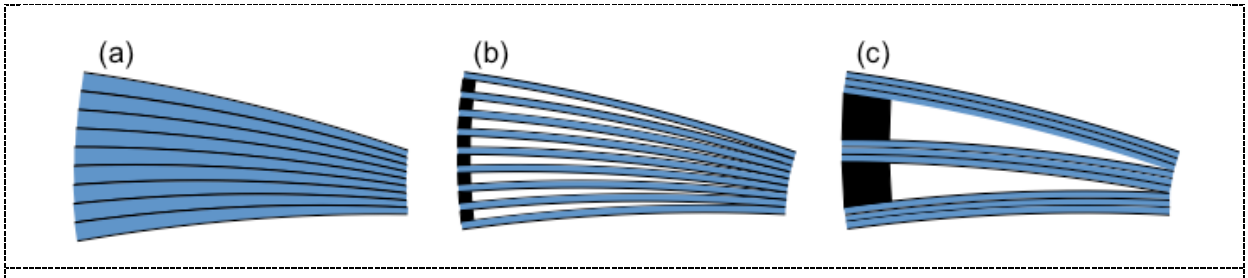

Figure 6. Possible channel arrangements for the convergent C-bender: wedge-type channels (a), plane-parallel channels with spacers at the entrance between each channel (b), channels grouped in blocks with spacers between blocks (c). (The gaps are largely exaggerated in this schematic picture.)

The results of the simulations are shown in figure 7. Here $P = \frac{N_\uparrow - N_\downarrow}{N_\uparrow + N_\downarrow}$ is the polarization of the outgoing neutron beam, $T = \frac{N_{total}^{out}}{N_{total}^{in}}$ - total transmission of initially unpolarized beam through the bender, $Q=P^2T$ - the figure of merit (also called the quality factor) commonly used for the characterization of polarizing devices [16-18]. However, for weak signals $Q=P^2T$ is not a good criteria anymore and one should better use the neutron beam with a high polarization.

The first important conclusion is that for the selected bender parameters the difference between benders with wedge-type and plane-parallel channels is negligible. From pure geometrical considerations one could expects the difference in transmission of 4.5% for C-benders, and 7.4% for S-benders. However, real numbers are even smaller (less than 3.5% and 5%, respectively), because the wedge-type channels accept smaller beam divergence (the same effect manifests itself as the reduction of the characteristic wavelength discussed in Section 2).

Among all analyzed options, the best polarization of the neutron beam is provided by the solid-state S-bender, owing to the highest number of reflections in the channels. The polarization of the solid-state C-bender is about 1% (2% for long wavelengths) worse than for the present-day bender, but still at a high level above 97%. At the same time, the transmission of the present-day is considerably lower than the one for C- and S-benders. Moreover, the transmission of the C-bender is 30% higher than for the S-bender. Therefore, the figure of merit $Q=P^2T$ is dominated by the transmission and demonstrates the clear superiority of the solid-state C-bender.

Beside the polarization and transmission of the benders, it is also important to watch the neutron intensity at the sample position. Figure 8 shows the distribution of the neutron flux across the beam for the above-discussed benders at three characteristic wavelength values of 6, 4.2 and 2 Å. The wavelength dependencies of the peak width, amplitude and integrated intensity are presented in the figure 9.

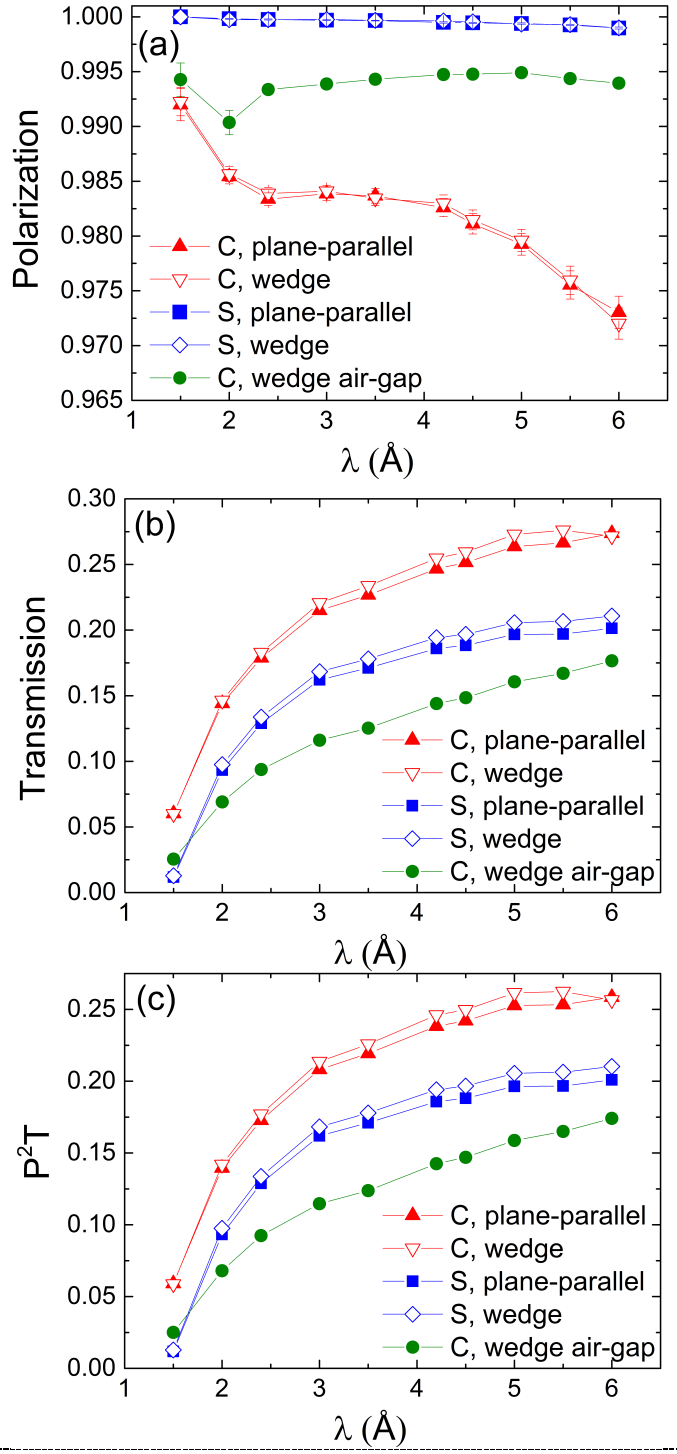

Figure 7. Main results of the simulation for different solid-state benders (see details in the text) in comparison with present-day air-gap bender: (a) transmission T, (b) polarization P, (c) quality factor P^2T. Where not shown, the error bars are within the size of the symbol. The transmission has been calculated as the ratio of the number of neutrons at the exit to the *total* number of neutrons (i.e. the both spin states) at the entrance of the polarizing bender.

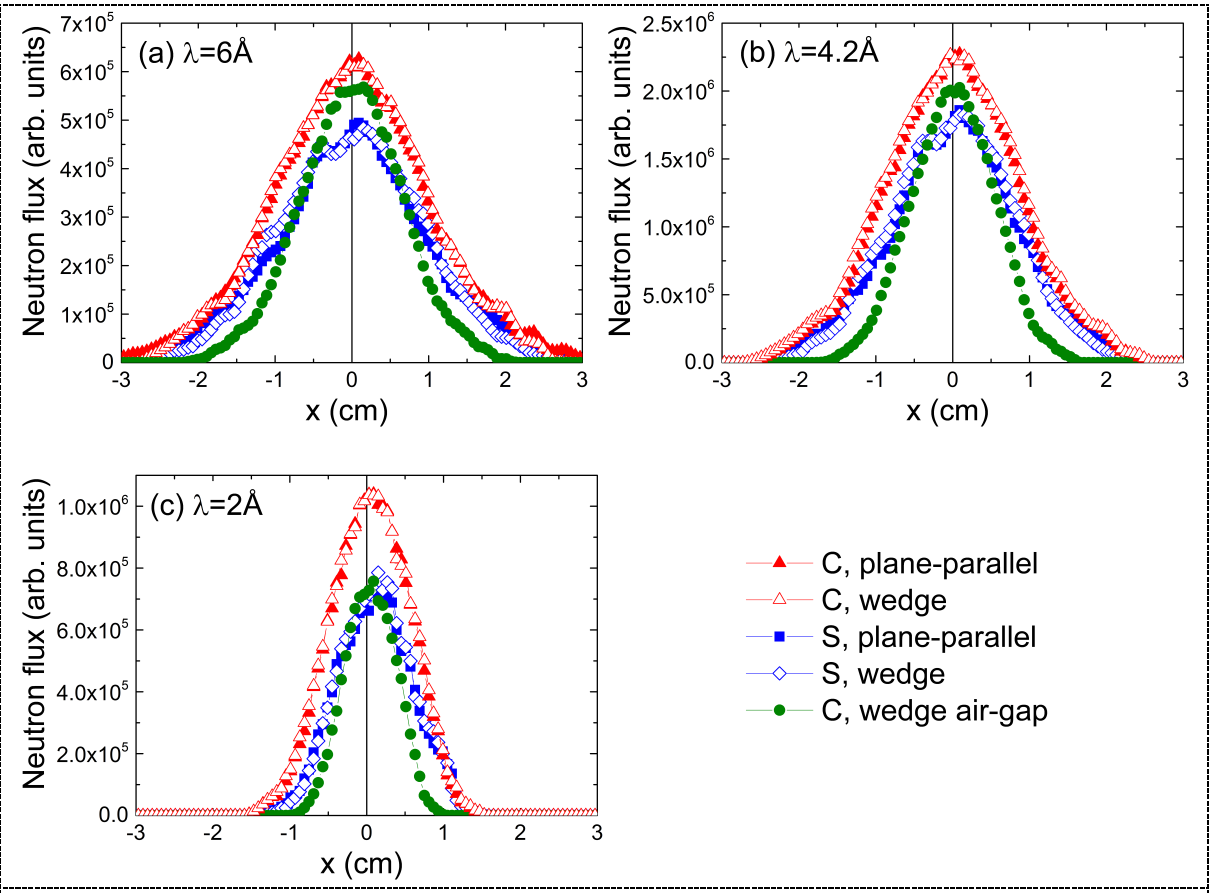

Figure 8. Neutron flux at the sample position for different benders at λ = 6 Å (a), λ = 4.2 Å (b) and λ = 2 Å (c). Neutron flux is integrated over the full beam height and shown as a distribution across the beam along horizontal x-axis perpendicular to the beam direction.

One can see that considered benders provide different beam size at the sample position. The smallest one can be achieved with present-day bender because it accepts the least angle divergence due to the lower value of $m = 2.7$, and has the largest length (in certain sense the polarizing bender serves also as a neutron guide). For the shortest solid-state C-benders with $m = 3.5$ the beam at the sample position is ~30% wider, whereas the S-benders with intermediate length demonstrate the values of the beam width between the present-day air-gap and solid-state C-bender. The effect of accepted divergence is clearly seen in the difference between solid-state benders of the same type with wedge-type and plane-parallel channels (for the bender with wedge-type channels the accepted divergence is higher). On the other side, for all bender we observe the increase of the beam size at the sample governed by the growth of the incoming beam divergence along with increase of the wavelength.

Due to the large beam width, the numbers of the intensity gain obtained above for the solid-state benders might be overestimated. To get more accurate numbers one has to analyze carefully beam distribution at the sample position. In agreement with transmission results, the highest peak amplitude is realized for the solid-state C-benders (figure 9b). Notably, this value is strongly dependent on the neutron wavelength. It has a clear maximum around 3-3.5 Å, corresponding to the spectral maximum in the flux coming to the monochromator.

In order to exclude the uncertainty related to the spectrum of the neutron source, in figure 9c we present the amplitude normalized to the incoming flux. Here, after the sharp increase at the short

wavelengths, the curve is nearly constant, with some decay at long wavelengths because of the beam spreading over a larger area due to higher divergence. The gain in respect to the air-gap bender is almost 40% at λ = 2 Å but only 10% at 6 Å.

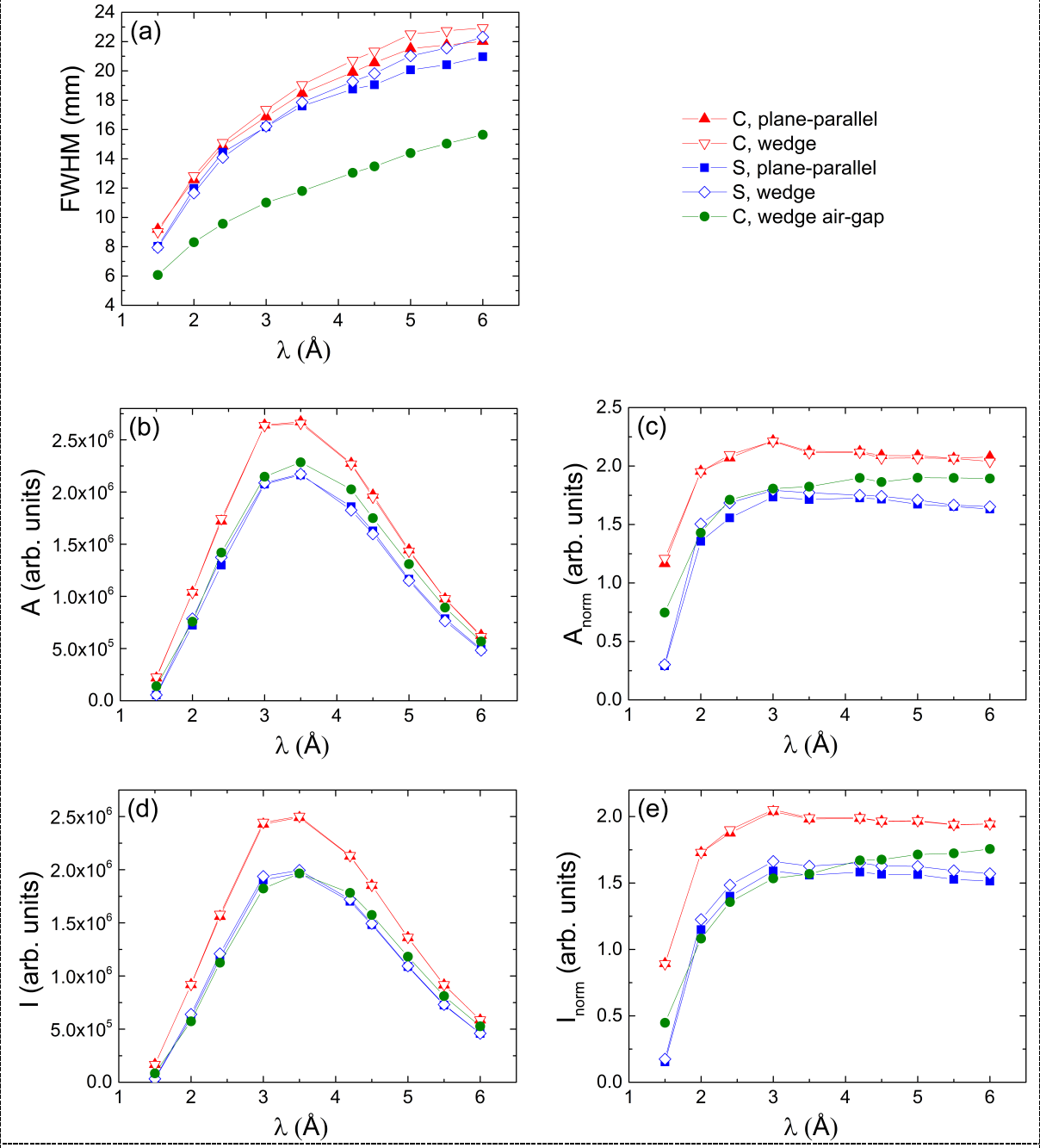

Figure 9. Parameters of the neutron flux distribution at the sample position as a function of neutron wavelength (neutron flux is integrated over the full beam height) for different benders: (a) the width (FWHM) of the distribution across the beam along horizontal x-axis perpendicular to the beam direction, (b) peak amplitude, (c) peak amplitude normalized to the wavelength dependence of the incoming flux, (d) intensity integrated over the range of 10mm in horizontal direction, (e) intensity integrated over the range of 10mm in horizontal direction and normalized to the wavelength dependence of the incoming flux.

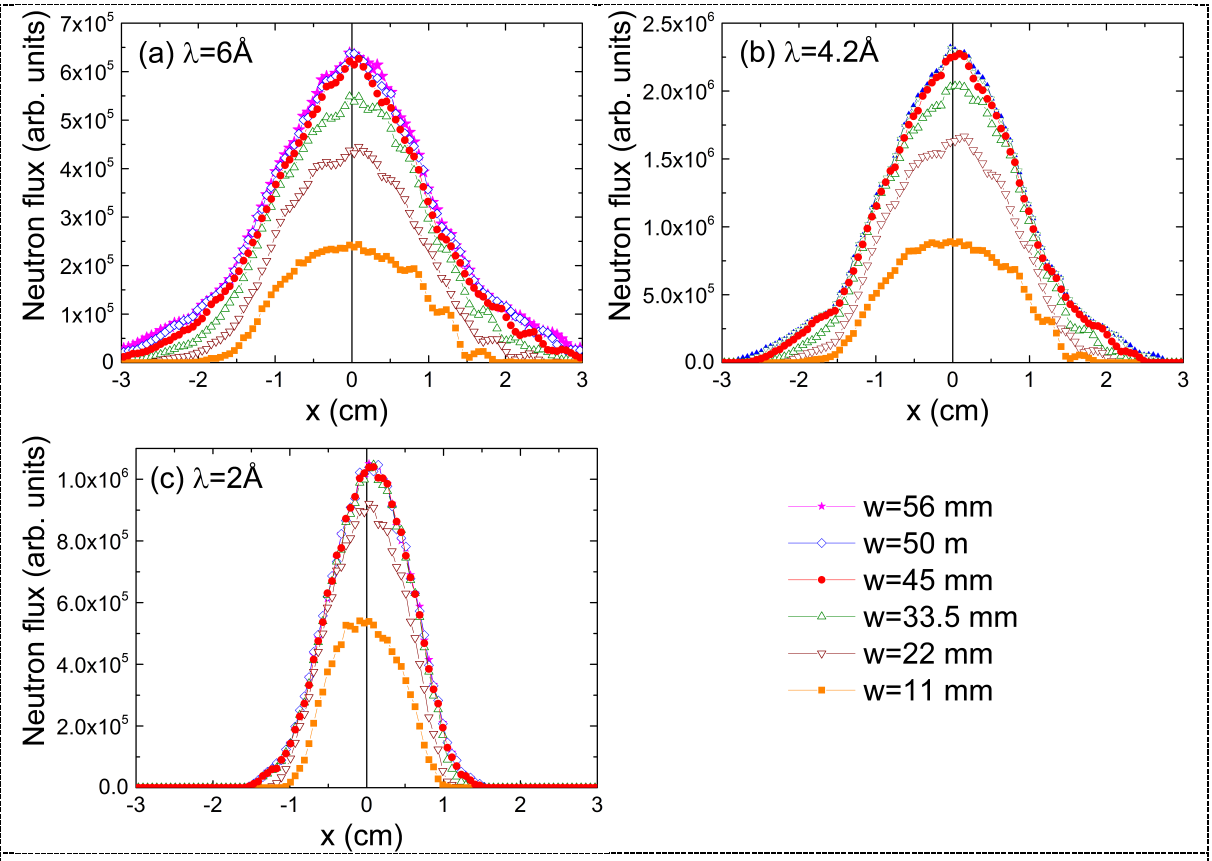

Figure 10. Influence of the width of C-bender with plane-parallel channels on the neutron flux at the sample position for λ = 6 Å (a), λ = 4.2 Å (b) and λ = 2 Å (c). Neutron flux is integrated over the full beam height and shown as a distribution across the beam along horizontal x-axis perpendicular to the beam direction.

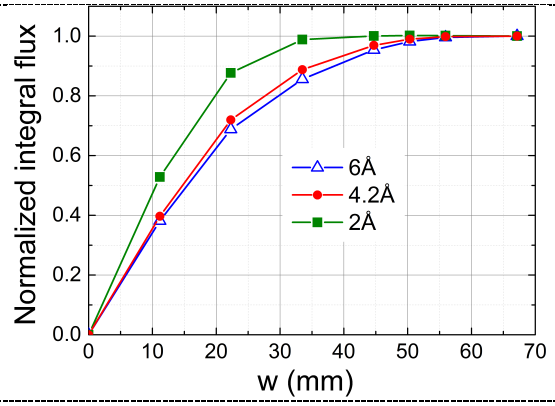

Figure 11. Dependence of the integral neutron flux at the sample position on the width of the C-bender with plane-parallel channels for several typical wavelength values. Neutron flux is integrated over the full beam height in vertical direction and over the range of 10 mm in horizontal direction, and then normalized for each wavelength to the unity at the maximum considered bender width.

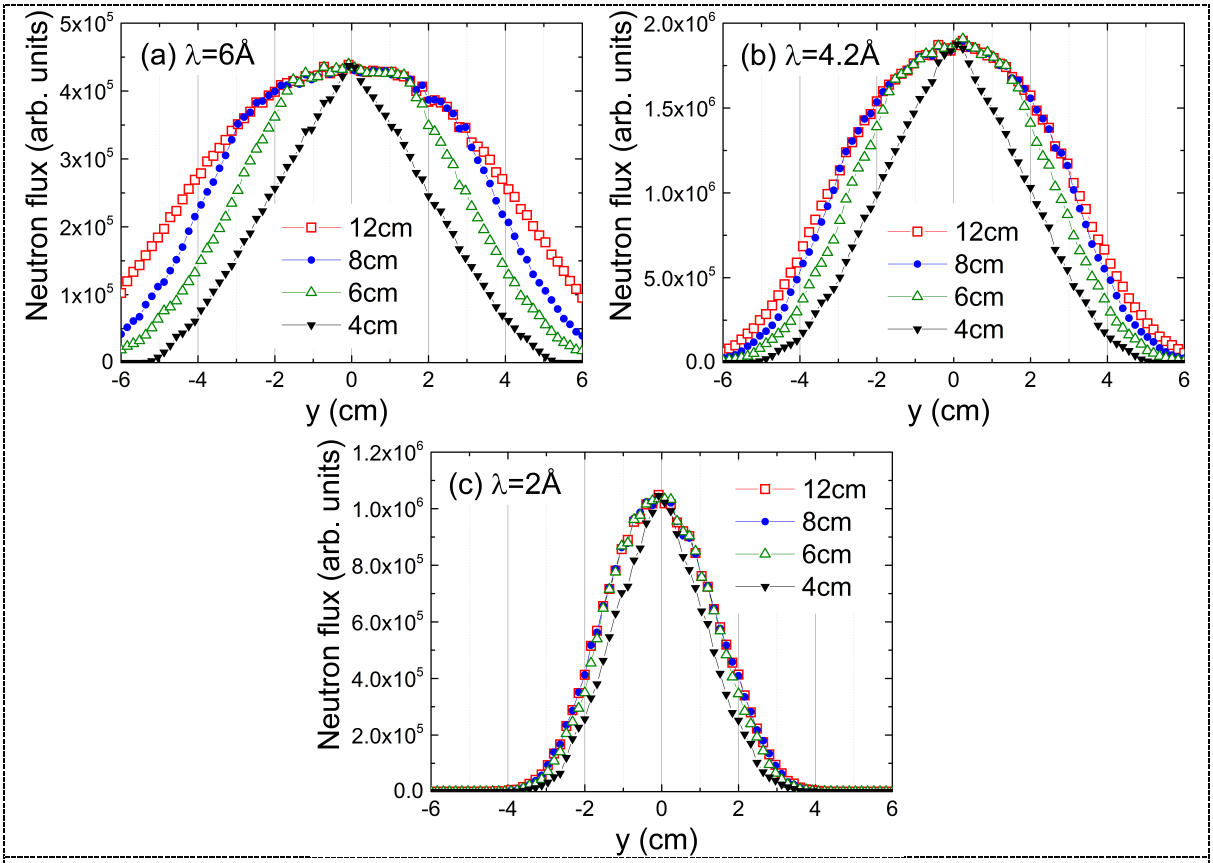

Figure 12. Influence of the height of C-bender with plane-parallel channels on the neutron flux at the sample position for λ = 6 Å (a), λ = 4.2 Å (b) and λ = 2 Å (c). Neutron flux is integrated over the full beam width and shown as a distribution across the beam along vertical y-axis perpendicular to the beam direction.

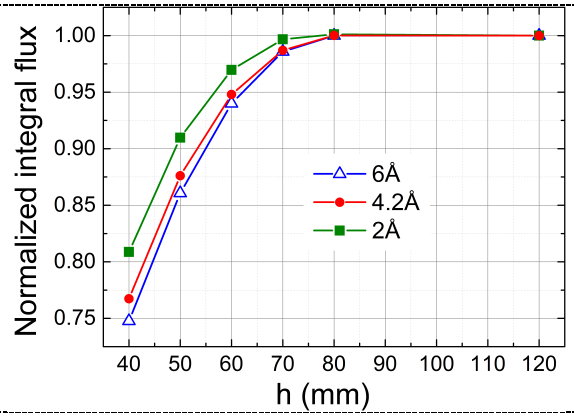

Figure 13. Dependence of the integral neutron flux at the sample position on the height of the C-bender with plane-parallel channels for several typical wavelength values. Neutron flux is integrated over the full beam width in horizontal direction and over the range of 60 mm in vertical direction, and then normalized for each wavelength to the unity at the maximum considered bender height.

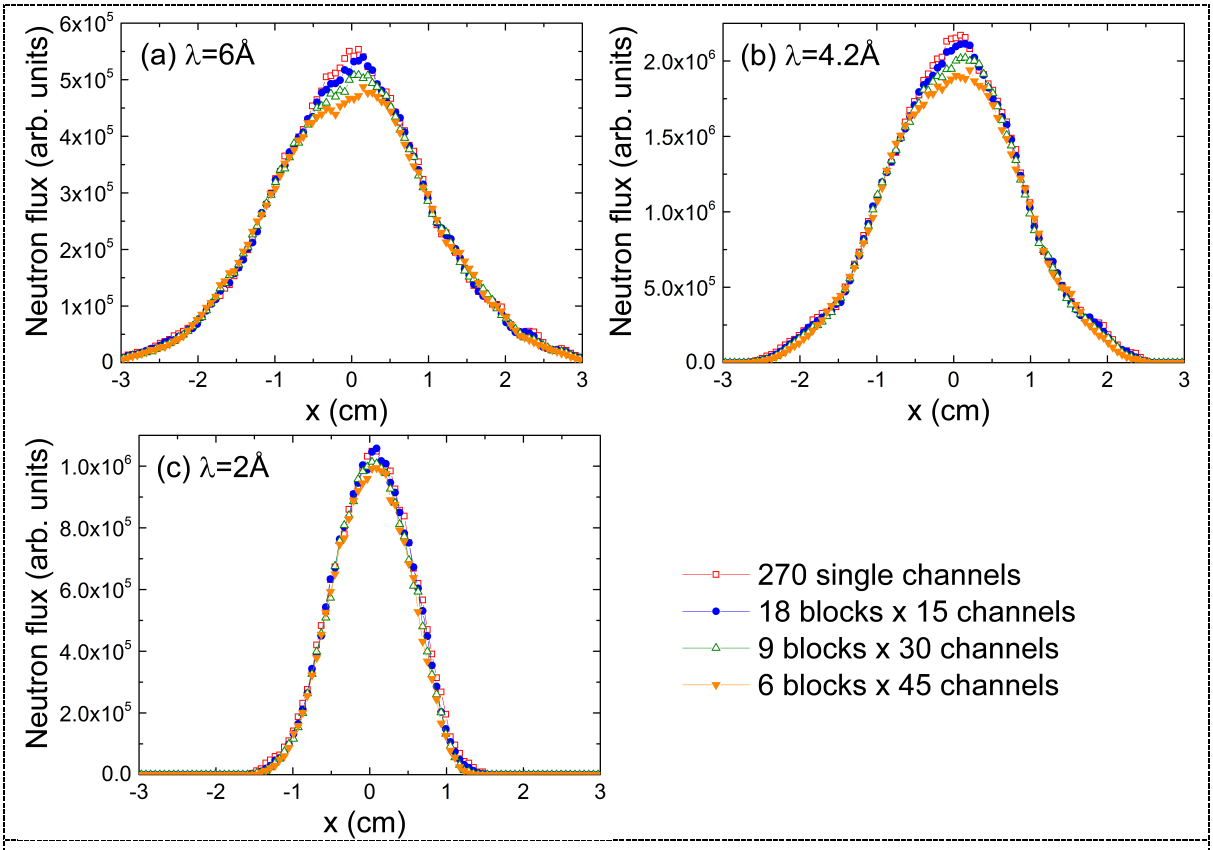

Figure 14. Neutron flux distributions at the sample position for the C-bender with the channel grouping. Neutron flux is integrated over the full beam height and shown as a distribution across the beam along horizontal x-axis perpendicular to the beam direction.

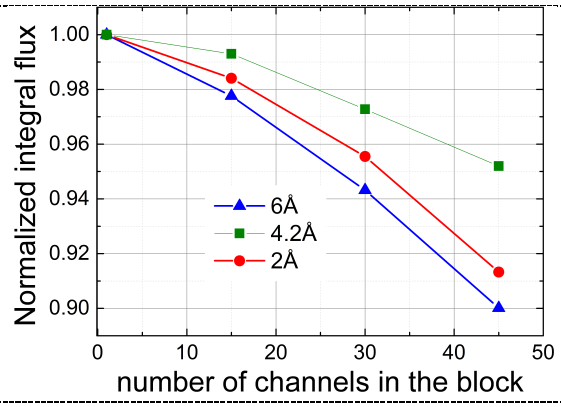

Figure 15. Dependence of the integral neutron flux at the sample position on the number of channels in the block (the number of channels is fixed to be 270). The neutron flux is integrated over the full beam height and 10 mm width, and normalized to unity for the case of the bender with single channels (figure 6b)

To get more accurate estimations, one has to integrate the intensity around the center of the beam over the typical sample width (10 mm at DNS). It is especially important for the short wavelength limit, where the present-day DNS bender cannot provide large enough beam size at the sample position. The larger beam width allows for the increase of the integral flux at the sample. Finally, for a typical experiment with the solid-state C-bender the gain in the integral intensity varies from 60% at $\lambda = 2$ Å to 10% at $\lambda = 6$ Å. In the long wavelength limit integration does not change the numbers because of the already sufficiently large beam size resulted from a large beam divergence at the exit from the neutron guide.

For the solid-state S-benders, despite of some gain in total transmission in respect to the present-day bender, the neutron flux at the sample is quite close to the present-day configuration, with some small gain or loss, depending on the neutron wavelength (see figure 9e). Thus, we can undoubtedly confirm the superiority of the solid-state C-bender.

For the practical realization of such bender, it is necessary to find the optimal width and height as the larger sizes leads to higher costs as well as extra complications in manufacturing. The influence of the bender width *w* on the neutron flux distribution at the sample position is presented in the figure 10. The dependence of the intensity at the 10 mm wide sample is shown in figure 11. One can see that for the bender with *w*=45mm intensity losses of about 5% are observed for longer wavelengths 4.2 Å and 6Å, whereas for short wavelength of 2 Å the losses are only about 1%. Indeed, the bender with a width of 45 mm is chosen for DNS as a reasonable compromise between the performance and costs.

A similar analysis has been carried out for the bender height *h* (figure 12). The reduction of the bender height gives rise to the cropping of the wings of the intensity distribution and subsequently to the intensity losses (see figure 13). However, since the maximum sample height at DNS is around 60mm (though usually does not exceed 40 mm), the height of the bender can be reduced down to 80 mm without any losses of the flux. Note, that the bender with *h*=40 mm limits the divergence of the beam delivered by the focusing monochromator and therefore the corresponding transmission profiles have a triangular shape that is typical for a slit collimation.

On the same reasons as for the width and the height, costs and complexity of manufacturing, it seems reasonable to reduce the number of spacers by combining several silicon wafers in a single block without using spacers, and place spacers between such blocks (see figure 6c). Below we present the optimization of these parameters for the C-bender with plane-parallel channels.

The results of simulations for the C-bender consisting of 270 channels (wafers) grouped in 18 blocks by 15 channels, 9 blocks by 30 channels, 6 blocks by 45 channels are presented in figures 14, 15. In general, the influence of grouped wafers is similar to the reduction of the bender width, with the most pronounced effect at the long wavelength. With 18 blocks by 15 wafers the integrated intensity is reduced by 2% in the worst case of $\lambda = 6$ Å, which is still acceptable.

4. Conclusion

The performance of the focusing polarizing benders illuminated by a convergent neutron beam reflected from focusing crystal monochromators has been considered. In sense of total transmission, the solid state S-bender is found to be inferior to the solid state C-bender due to the shorter neutron path in silicon, but still better than the Schärpf-type air-gap bender. However, taking into account the real sample size, our simulations unambiguously demonstrate the superiority of the focusing solid-state C-bender with respect to both Schärpf-type and solid-state S-benders.

We have analyzed the performance of a C-bender with a reduced number of spacers, when several silicon wafers are combined in the blocks, which may significantly simplify the manufacturing process. Though it will generally result in extra losses in the transmission of the bender, the losses may be tolerated if the number of wafers in the blocks is not too large; e.g. grouping together 15 wafers reduces the bender transmission only by 2%.

Finally, we consider the solid-state C-bender with Fe/Si coating m=3.5 as the optimal solution for a new polarizer at DNS. Such bender is much more compact than the present-day air-gap Schärpf-type bender (55 mm against 290 mm) and provides the intensity gain from 10% to 60% at the 10mm sample (depending on the wavelength) by the cost of slightly lower polarization (97-98.5% against 99.5%).

Acknowledgments
We would like to thank S. Manoshin (JINR, Russia), M. Khaneft, S. Mattauch, N. Violini, Z. Salhi (all JCNS) and Th. Krist (HZB) for useful discussions.

References

[1] Schweika W, Böni P 2001 Physica B **297** 155-159
[2] Su Y, Nemkovskiy K and Demirdiş S 2015 JLSRF **1** A27 1-4
[3] Schaerpf O 1989 Physica B **156&157** 639-646
[4] Hahn W, Schweika W 1997 Physica B **234** 1165-1167
[5] Böni P, 1996 J. Neutron Res. **5** 63-70
[6] Böni P, Clemens D, Senthil Kumar M, Pappas C 1999 Physica B **267-268** 320-327
[7] Krist Th, Kennedy S J, Hicks T J, Mezej F 1998 Physica B **241-243** 82-85
[8] Stunault A, Andersen K H, Roux S, Bigault T, Ben-Saidane K, Rønnow H M 2006 Physica B **385–386** 1152–1154
[9] Krist Th, Rucker F, Brandl G, Georgii R 2013 Nucl. Instr. Meth. Phys. Res. A **698** 94-97
[10] Shah V R, Washington A L, Stonaha P, Ashkar R, Kaiser H, Krist T, Pynn R 2014 Nucl. Instr. Meth. Phys. Res. A **768** 157-163
[11] Majkrzak C F, Nunez V, Copley J R D, Ankner J F, and Greene G C 1992 Proc. SPIE **1738** 90
[12] Hayter J B, Penfold J, Williams W G 1978 J. phys. E: Sci. Instrum. **11** 454-458
[13] http://www.helmholtz-berlin.de/forschung/oe/em/transport-phenomena/projekte/vitess/index_en.html
[14] http://www.swissneutronics.ch/index.php?id=24
[15] Freund A K 1983 Nucl. Instr. Meth. **213** 495-501
[16] William W G 1973 Rutherford Appleton Laboratory Report **RL-73-034**
[17] Gussen L D 1998 J. Neutr. Res. **7** 15-37
[18] Goossens D J, Cussen L D 2002 Nucl. Instr. Meth. A **481** 475-492